

# Optimization of dual-layer flow field in a water electrolyzer using a data-driven surrogate model

Lizhen Wu<sup>a</sup>, Zhefei Pan<sup>c,d</sup>, Shu Yuan<sup>e</sup>, Xiaoyu Huo<sup>a</sup>, Qiang Zheng<sup>f,\*</sup>, Xiaohui Yan<sup>e,\*</sup>, Liang An<sup>a,b,\*</sup>

<sup>a</sup> Department of Mechanical Engineering, The Hong Kong Polytechnic University, Hung Hom, Kowloon, Hong Kong, China

<sup>b</sup> Research Institute for Sports Science and Technology, The Hong Kong Polytechnic University, Hung Hom, Kowloon, Hong Kong, China

<sup>c</sup> Key Laboratory of Low-grade Energy Utilization Technologies and Systems (Chongqing University), Ministry of Education, Chongqing, 400030, China

<sup>d</sup> Institute of Engineering Thermophysics, Chongqing University, Chongqing 400030, China

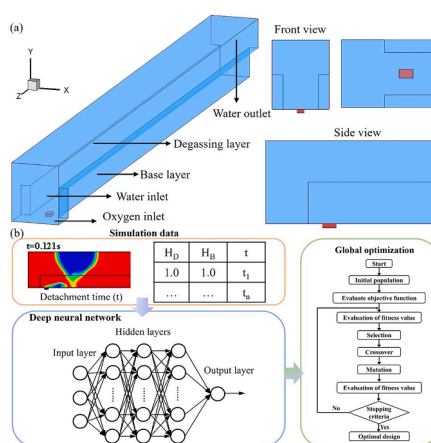
<sup>e</sup> Institute of Fuel Cells, School of Mechanical Engineering, Shanghai Jiao Tong University, 800 Dongchuan Road, Shanghai 200240, China

<sup>f</sup> Eastern Institute for Advanced Study, Eastern Institute of Technology, Ningbo, Zhejiang 315200, China

## HIGHLIGHTS

- VOF method is utilized to investigate the effects of different degassing layer and base heights on the bubble behavior in channel.
- The optimization framework combing DNN and GA is conducted to accelerate the optimization of flow field.
- The reliability of the optimization scheme is validated by bubble visualization and electrochemical characterization.

## GRAPHICAL ABSTRACT



## ARTICLE INFO

### Keywords:

PEMWE  
Dual-layer flow field  
Data-driven surrogate model  
Machine learning

## ABSTRACT

Serious bubble clogging in flow-field channels will hinder the water supply to the electrode of proton exchange membrane water electrolyzer (PEMWE), deteriorating the cell performance. In order to address this issue, the dual-layer flow field design has been proposed in our previous study. In this study, the VOF (volume of fluid) method is utilized to investigate the effects of different degassing layer and base heights on the bubble behavior in channel and determine the time for the bubbles to detach from the electrode surface. However, it is very time-consuming to get the optimal combination of base layer and degassing layer heights due to the large number of potential cases, which needs to be calculated through computation-intensive physical model. Therefore, machine learning methods are adopted to accelerate the optimization. A data-driven surrogate model based on deep

\* Corresponding authors.

E-mail addresses: [qzheng@eitech.edu.cn](mailto:qzheng@eitech.edu.cn) (Q. Zheng), [yanxiaohui@sjtu.edu.cn](mailto:yanxiaohui@sjtu.edu.cn) (X. Yan), [liang.an@polyu.edu.hk](mailto:liang.an@polyu.edu.hk) (L. An).

<https://doi.org/10.1016/j.egyai.2024.100411>

Available online 21 August 2024

2666-5468/© 2024 The Author(s). Published by Elsevier Ltd. This is an open access article under the CC BY-NC license (<http://creativecommons.org/licenses/by-nc/4.0/>).

neural network (DNN) is developed and successfully trained using data obtained by the physical VOF method. Based on the highly efficient surrogate, genetic algorithm (GA) is further utilized to determine the optimal heights of base layer and degassing layer. Finally, the reliability of the optimization was validated by bubble visualization in channel and electrochemical characterization in PEMWE through experiments.

## 1. Introduction

Water electrolysis technologies can be coupled with renewable electricity to produce green hydrogen, which will help meet energy and climate goals by 2030 [1], and may even have a high probability of achieving climate neutrality by 2050 due to its zero carbon emissions [2]. Among the different types of water electrolysis technologies, proton exchange membrane water electrolyzer (PEMWE) has received more and more attention in recent years due to its advantages of high current density operation, high purity of hydrogen production, etc. [3–5].

Fig. 1 shows the typical PEMWE and its working principle. There are complex multi-physics fields coupling of gas-water-thermal-electricity in PEMWE. Among them, poor mass transport in anode under the high current density is a very critical issue to limit the performance of PEMWE [6,7] and the influence of the hydrogen evolution reaction (HER) at cathode can generally be ignored [8]. When energizing the PEMWE and feeding water to the anode inlet, three processes occur sequentially, including bubble evolution reaction (OER) in anode catalyst layer (CL), bubble transports inside the anode porous transport layer (PTL) and bubble flow in anode flow field [9]. They influence each other and serious bubble clogging in channel such as slug and plug flows will cover the outer surface of the electrode [10,11], thus hindering the water delivery to the anode CL, which are more significant with the increasing current density [12]. Thus, the anode flow field design and optimization are the important areas in PEMWE development.

As the only connection to the outside for the reactants and products inside PEMWE system, the flow-field channels not only ensure the supply of liquid water to the electrodes, but also discharge the gas products (bubbles) in a timely manner. Conventional parallel and serpentine flow fields are the most common flow field adopted in PEMWE [11]. While they possess the advantage of simple fabrication [6], they often experience severe bubble clogging in the channel, especially at high current densities. For example, meandering and tortuous structure of serpentine flow field can create stagnation zones that lead to bubble clogging, resulting in worse performance in PEMWE than that

with parallel flow field [13]. Novel flow fields mainly include optimization based on conventional channel-rib structure and application of porous structure. As for the novel flow fields, electrochemical measurements combined with in-situ optical visualization can be an effective tool [14] to visualize the bubbles behaviors in flow field and build the relationship between them. For example, in our previous work [15], a dual-layer flow field design consists of an upper degassing layer with a larger width on the lower base layer in contact with the electrodes. Experimentally, it is observed that more electrode surfaces are exposed to water, and the cell performance is significantly upgraded by about 0.15 V at  $5.0 \text{ A cm}^{-2}$ . Wang et al. [16] demonstrated the ability of interdigitated-jet hole flow field (IJFF) to enhance bubble removal and improve under-rib convection through two-phase flow visualization and numerical simulation. As for some special flow fields such as pin-type, porous metal expanded mesh, etc., it is difficult to visualize two-phase flow in flow field with a special transparent cell. Thus, numerical simulation [17,18] is also considered as a powerful tool to optimize the flow-field designs due to the ability of including complex and detailed geometry structure. For example, Khatib et al. [19] investigated the effect of serpentine, mesh and open pore cellular foams (OPCF) on PEMWE using a 3D model, and the simulation results showed that the performance of the PEMWE assembled with OPCF was 1.5 times higher than that with the mesh channel.

In addition, for optimizing the critical components of PEMWE, a large number of cases are required to obtain an optimized solution either using experimental or numerical simulation methods. It is not only resource-intensive, but also very time-consuming [20]. In order to address these issues, the integration of artificial intelligence (AI) techniques in novel structure design discovery, fabrication, and optimization can greatly accelerate the progress [21–23]. Currently, data-driven surrogate models based on machine learning methods are very popular in the field of PEM fuel cells [24,25] and have been gradually applied to PEMWE design. For example, Hayatzadeh et al. [26] optimized the operating conditions for extending lifespan and reducing hydrogen production costs of PEMWE by coupling experimental tests, support

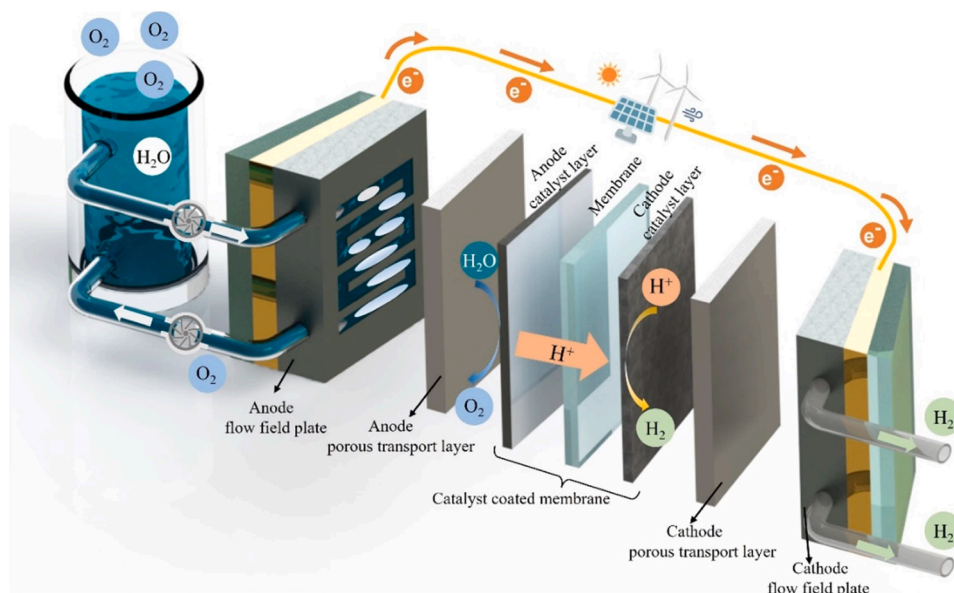


Fig. 1. Working principle of a PEMWE.

vector regression (SVR) and genetic algorithm (GA). Yang et al. [27] collected 1062 experimental data from top-notch publications. After that, k-nearest neighbor (KNN) and decision tree regression (DRT) models were used to determine the optimal flow flow-path design in a PEMWE. Chen et al. [28] combined a multi-physics coupling model with a data-driven surrogate model (i.e., the artificial neural network (ANN)) to obtain the optimal channel width and depth of 2 mm, achieving a 38.61% increase in current density. Therefore, the combination of experimental tests or physical models and machine learning methods will likely become a mainstream method in optimization of critical components in PEMWE.

In this work, based on the dual-layer design we have proposed, as shown in Fig. 2. The VOF method is adopted to investigate the effects of different degassing layer and base heights on the bubble behavior in channel and determine the time for the bubbles to detach from the electrode surface. Afterwards, the simulation data including diversified scenarios are collected to build a surrogate model by using DNN, which then can be used to give performance predictions very efficiently. Based on the surrogate, GA is further utilized to determine the optimal combination of base layer and degassing layer heights. Finally, the reliability of the optimization scheme is validated by bubble visualization in channel and electrochemical characterization in water electrolyzer through experiments. Therefore, this work provides an optimized flow-field design to rapidly discharge bubbles from the channels of water electrolyzer.

## 2. Methods

### 2.1. Optimization framework

Fig. 3(a) depicts the computational domain in the physical model with the dual-layer design flow channel consisting of a degassing layer and a base layer. Fig. 3(b) shows the optimization scheme of the dual-layer flow channel design. The time for a bubble to detach from the electrode surface is defined as detachment time, which affects the electrochemical performance of PEMWE. In this study, the fastest bubble detachment time from the electrode surface is chosen as the optimization objective. The framework of this work can be summarized in the following steps: (1) Physical model is used to explore the effect of

degassing layer and base layer heights on bubble detachment time at different oxygen velocities, and the simulation results constitute a database. In physical model, the moment when the oxygen volume fraction at the electrode surface reaches 0 is considered to be the bubble detachment time. (2) A surrogate model is obtained by using a data-driven method based on the generated database, and the accuracy of the trained surrogate model is validated in a new testing database. Thus, the validated surrogate model can replace the physical model to effectively predict the bubble detachment time in new scenarios. (3) We use the surrogate model and the stochastic optimization algorithm to search for the optimal combination of degassing layer and base layer heights for the minimal bubble detachment time. (4) The optimal solutions are verified by the electrochemical tests and two-phase flow visualization of the flow field.

#### 2.1.1. Physical model

An oxygen inlet is set at the bottom of the channel to simulate the single bubble behavior (detaching from the electrode surface), as shown in Fig. 3(a). The bottom wall represents the electrode surface, and other walls represent internal surfaces of the flow channel. VOF method [29, 30] is adopted to track the two-phase interface between liquid water and oxygen. The liquid water and oxygen are regarded as the primary phase and the second phase, respectively. The relevant governing equations are shown in Table 1. where  $\rho_m$  ( $\text{kg m}^{-3}$ ) is the density,  $u_m$  ( $\text{m s}^{-1}$ ) the velocity vector,  $P$  (Pa) the static pressure,  $\mu_m$  ( $\text{kg m}^{-1} \text{s}^{-1}$ ) the viscosity,  $g$  ( $9.8 \text{ m s}^{-2}$ ) the gravitational constant and  $F_s$  ( $\text{N m}^{-3}$ ) the source term corresponding to the surface tension effect, the subscript m stands for gas-liquid mixture.

The continuous surface force (CSF) model is used for the inclusion of surface tension:

$$F_s = \sigma k \delta(\mathbf{r} - \mathbf{r}_{int}) \vec{n} \quad (1)$$

$$k = -\nabla \cdot \vec{n} = -\nabla \cdot \left( \frac{\nabla \alpha}{|\nabla \alpha|} \right) \quad (2)$$

$$\vec{n} = \vec{n}_w \cos \theta + \vec{t}_w \sin \theta \quad (3)$$

where  $\sigma$  ( $\text{N m}^{-1}$ ) is the surface tension coefficient,  $k$  the radius of

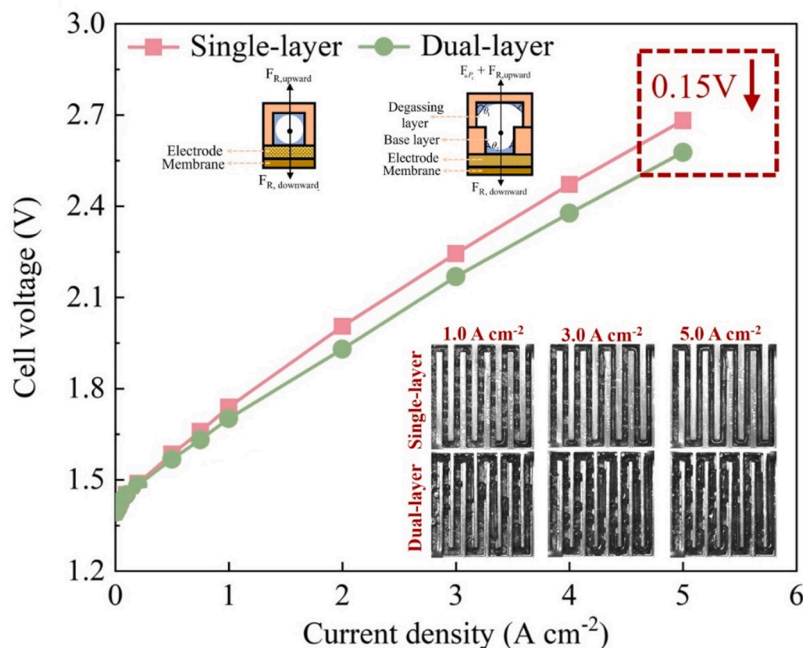


Fig. 2. Comparison of electrochemical performance of PEMWE assembled with single-layer and dual-layer flow field in our previous study [15].

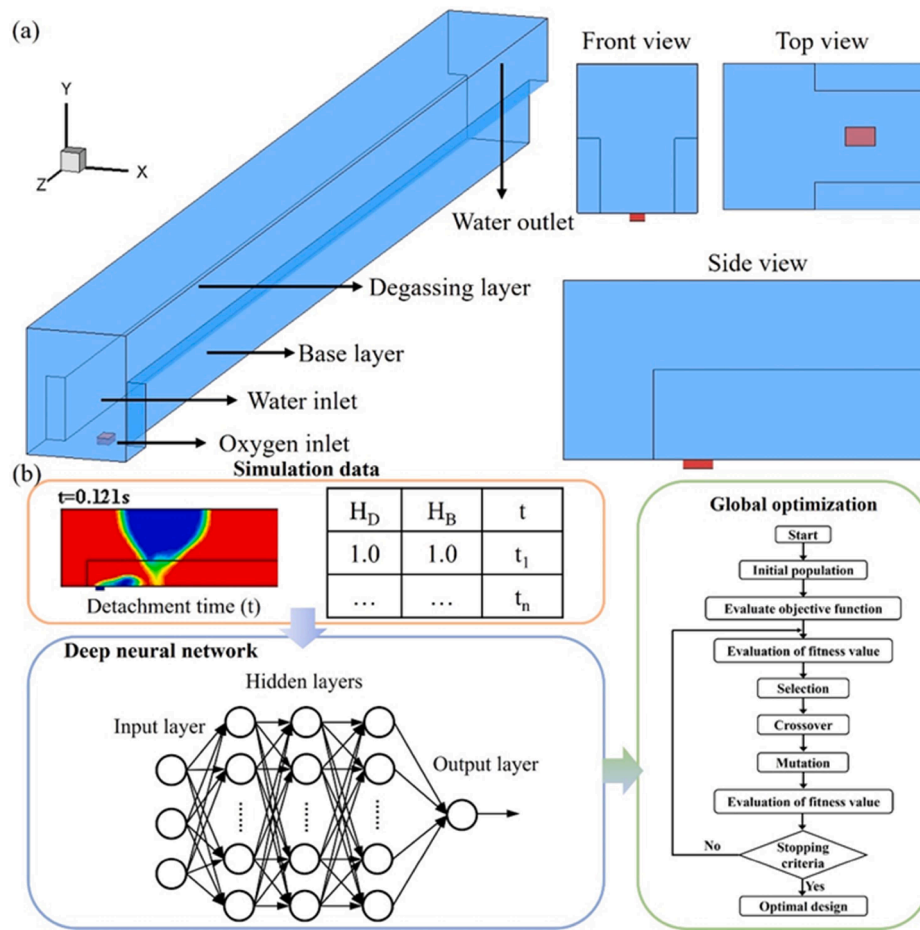


Fig. 3. (a) Computational domain in physical model and (b) optimization framework.

Table 1  
Governing equations.

Descriptions	Governing equations
Mass	$\frac{\partial \rho_m}{\partial t} + \nabla \cdot (\rho_m u_m) = 0$
Momentum	$\frac{\partial (\rho_m u_m)}{\partial t} + \nabla \cdot (\rho_m u_m u_m) = -\nabla P + \nabla \cdot [\mu_m (\nabla u_m + \nabla u_m^T)] + \rho_m g + F_s$
Gas phase volume fraction	$\frac{\partial s_g}{\partial t} + \nu \cdot \nabla s_g = 0$

curvature,  $\delta(\mathbf{r})$  the Dirac delta function,  $\vec{n}$  the unit normal vector at the interface,  $\vec{n}_w$  and  $\vec{t}_w$  the unit vectors normal and tangential to the channel wall, respectively, and  $\theta$  the contact angle at channel walls.

The important parameters are given in Table 2 and more details have been given in our previous studies [15]. Numerical procedures are

Table 2  
Geometry parameters and operation conditions.

Parameter	Value
Degassing layer width (mm)	1.6
Base layer height/width (mm)	1.0
Channel length (mm)	20
Liquid water velocity ( $\text{m s}^{-1}$ )	0.00174
Oxygen velocity ( $\text{m s}^{-1}$ )	1/3/5/10
Operation pressure (atm)	1.0
Operating temperature (K)	273.15
Contact angle of channel wall ( $^\circ$ )	70
Contact angle of electrode surface ( $^\circ$ )	30

implemented by the commercial computational fluid dynamics (CFD) software ANSYS FLUENT, and the involved equations are build-in. The same settings and key information can be found in [29,30].

### 2.1.2. Data-driven surrogate model

In this study, the adopted DNN, denoted as  $F$ , constitutes one input layer, three hidden layers and one output layer. Each hidden layer has 20 neurons and takes Rectified Linear Unit (ReLU) as the nonlinear activation function. The input layer has 3 neurons and the corresponding input variables are the oxygen velocity ( $v_{O_2}$ ), base layer height ( $H_B$ ) and degassing layer height ( $H_D$ ). The output layer has one single neuron to produce the bubble detachment time ( $T$ ). That is, the function relationship between bubble detachment time and oxygen velocity, base layer height and degassing layer height can be learned from data.

$$T = F(H_B, H_D, v_{O_2}) \quad (4)$$

In this study, a total of 66 data samples at various base layer heights, degassing layer heights and oxygen velocities are generated using the 3D physical model mentioned above, as shown in Supporting Information. We randomly select 80% of the whole dataset for training and 20% of that for testing. The DNN model is trained by adopting Adam optimizer [31] with learning rate as  $3e^{-3}$  for 4,000 epochs.

Once training is completed, the trained model can be used to efficiently and accurately give predictions in new scenarios. Owing to this excellent feature, we can use it to explore the design space and find the optimal combination of input variables (i.e.,  $v_{O_2}$ ,  $H_B$ , and  $H_D$ ) that minimize the output bubble detachment time. In this work, the genetic algorithm (GA), which is a widely-used global optimization method inspired by the process of natural selection, is leveraged to find the

optimal combination of inputs. We make use of Python package *scikit-opt* to realize GA by setting the population size as 100, the mutation probability as  $1e^{-3}$ , and the maximum iterations as 300 steps. The flowchart of DNN-based GA is illustrated in Fig. 3.

## 2.2. Experimental

### 2.2.1. PEMWE fabrication

The PEMWE fabrication is shown in Fig. 1. In order to observe the two-phase flow in flow field, the anode end plate with a visualization window and transparent acrylic plate achieve this function. The remaining components are consistent with common cells. Anode flow field plate (degassing layer and the base layer) is made of titanium (Ti). Ti felt with an  $0.5 \mu\text{m}$  Iridium (Ir) is used as the anode PTL. Its initial porosity is 0.6 and thickness is  $400 \mu\text{m}$ , respectively. The cathode PTL is

carbon paper (Toray, TGP-H-090). A commercial catalyst coated membrane (CCM) (from Anhui Contango New Energy Technology Co, Ltd.) is used in this study. It consists of a membrane of Nafion 115, an anode catalyst of  $\text{IrO}_2$  (the most commonly used OER catalyst [32,33]) with a loading of  $2.0 \text{ mg cm}^{-2}$ , and Pt/C (the most commonly used HER catalyst [34]) with a loading of  $1.0 \text{ mg cm}^{-2}$ . The active area of membrane electrode assembly (MEA) is  $4.0 \text{ cm}^2$  ( $2.0 \text{ cm} \times 2.0 \text{ cm}$ ). Fluorine rubber gaskets with thicknesses of  $0.4 \text{ mm}$  and  $0.3 \text{ mm}$  are used for the anode and cathode, respectively. The torque was set at  $4.5 \text{ N m}$  to assemble the cell.

### 2.2.2. Testing platform

A peristaltic pump (BT100-2J, LongerPump) supplied deionized water with  $80^\circ\text{C}$  into the anode inlet of the PEMWE at a mass flow rate of  $5 \text{ ml min}^{-1}$ . Temperature controller and thermocouples are used to

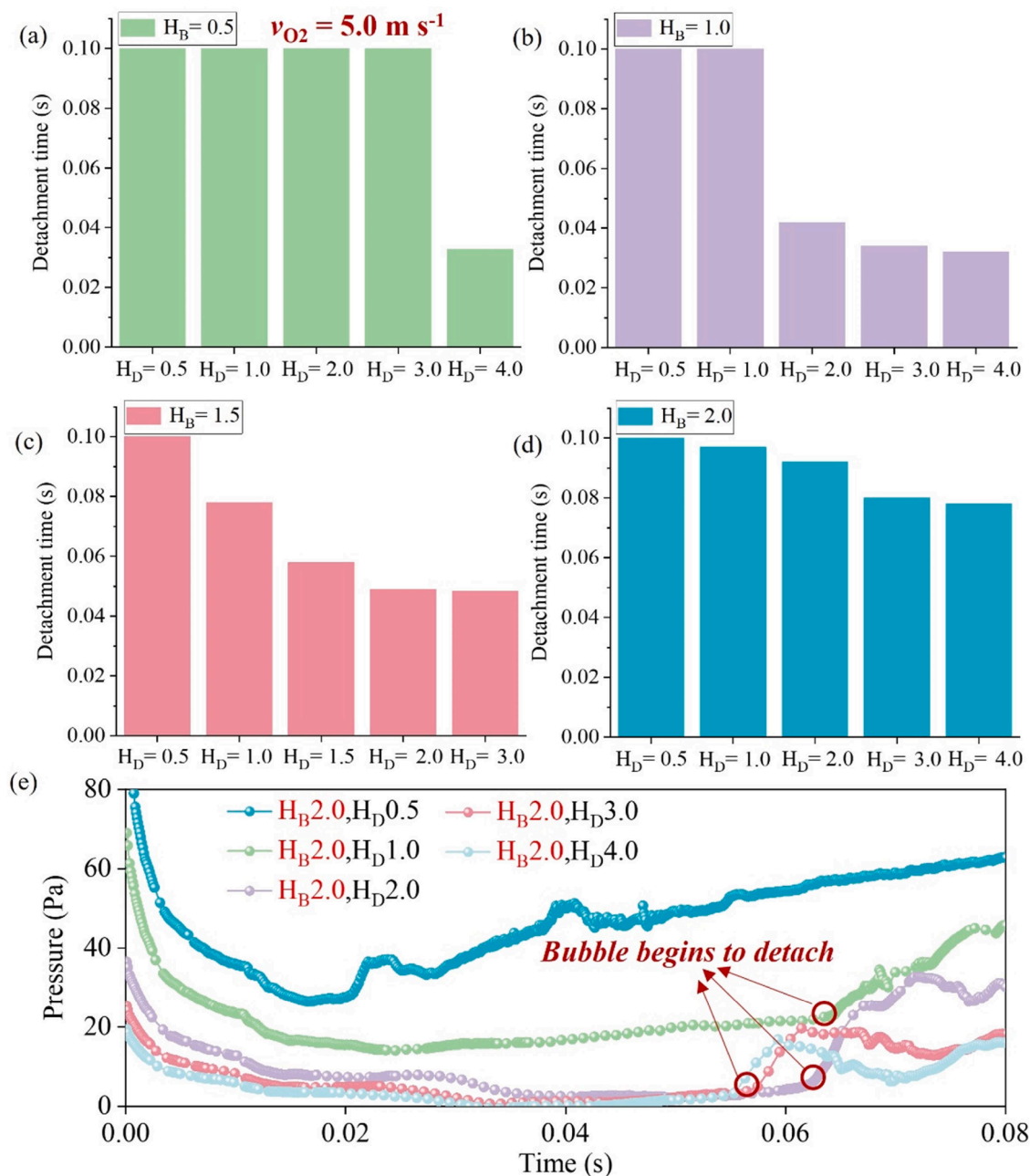


Fig. 4. Detachment time of bubbles from the electrode surface under the degassing layer with different heights: (a) base layer height (0.5 mm), (b) base layer height (1.0 mm), (c) base layer height (1.5 mm), (d) base layer height (2.0 mm), (e) the average pressure in middle plane of degassing layer.

maintain cell operation at 80 °C. For the polarization curve and electrochemical impedance spectroscopy (EIS) measurements, an Autolab PGSTAT302N electrochemical workstation with an add-on booster was used to characterize them. The PEMWE adopts galvanostatic mode. The PEMWE operates for 5 minutes at each current density to reach a stable state to measure the polarization curve within the current density range of 0 to 5.0 A cm<sup>-2</sup>. Finally, the data will be reliable by taking the average voltage value of the last 30 seconds at each operation set point. As for the EIS measurements, a sinusoidal current was adopted as the disturbance, and its amplitude and frequency range were 5% of the real-time current and 10 kHz to 0.1 Hz, respectively.

The whole high-speed visualization system includes Revealer M230M high-speed camera and microscale lens. In this study, a recording frame rate of 500 frame per second (fps) was chosen to record the two-phase flow in flow field at the current densities of 1.0 and 5.0 A

cm<sup>-2</sup>. More details can be found in our previous study [15].

### 3. Results and discussion

#### 3.1. Effect of geometry structure

The height of the base layer (0.5-2 mm) and the height of the degassing layer (0.5-4 mm) are adjusted, respectively. The VOF method is used to simulate the bubble detachment time for different combinations of base layer height and degassing layer height, as shown in Fig. 4 (a-d). With an oxygen velocity of 5 m s<sup>-1</sup>, the base layer is 0.5 mm and the bubble starts to detach from the electrode surface only when the degassing layer exceeds 3 mm. Therefore, the base layer needs to be high enough to avoid the bubble being attached to the electrode surface. When the base layer height is more than 0.5 mm, e.g., when the base

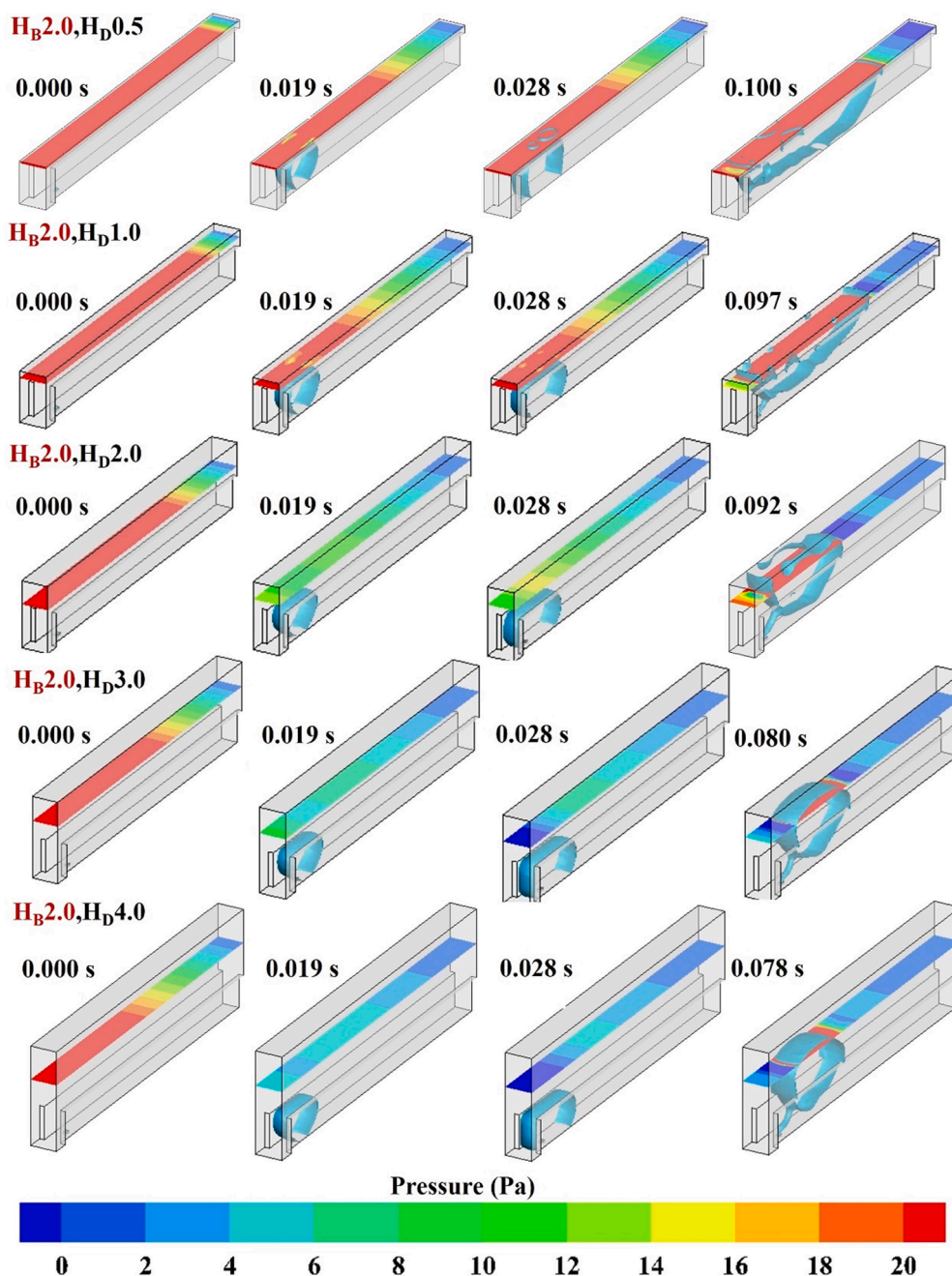


Fig. 5. The pressure distribution in the middle plane of degassing layer.

layer is fixed at 1 mm, the higher the degassing layer is, the shorter the bubble detachment time is. However, when the height of the degassing layer increases to 4 mm, the bubble detachment time does not decrease significantly compared to the scenario with 3 mm, which can be assumed that there is an optimal value for convergence. This is because bubbles detach from the electrode surface and enter the degassing layer from the base layer, which is dominated by two steps (Fig. 5): (1) the upper bubble surface enters the degassing layer, (2) the interfacial curvature of upper bubble surface decreases. With a fixed height of the base layer, the width of the degassing layer channel is also fixed at 1.6 mm (0.6 mm wider than the base layer channel), so the interface curvature decreases at a consistent rate (second step). The higher the degassing layer is (Fig. 4 (e)), the lower its water pressure will be and the time for the upper surface of the bubble to enter the degassing layer will be reduced (first step). After the upper surface of the bubble enters the degassing layer, the upper surface interfacial curvature decreases quickly and the self-pumping effect starts to act on that bubble, as shown in Fig. 5. The relative contours of bubble detachment time are also provided in Fig. S1 (Supporting Information).

The base layer height has a significant effect on the first step mentioned above and higher base layer will increase the time for the first step. Thus, for example, when the degassing layer is fixed at 2 mm, the higher the base layer is, the longer the bubble detachment time is. However, the increase in oxygen velocity reduces the effect of the base layer on the bubble detachment time. For example, with increasing oxygen velocity, the maximum difference caused by the base layer ( $v_{O_2} = 5 \text{ m s}^{-1}$ ) was 0.056 s and the maximum difference caused by the base

layer ( $v_{O_2} = 10 \text{ m s}^{-1}$ ) was 0.007 s when the height of the degassing layer was fixed at 3 mm. Therefore, in order to realize effective bubble removal at high current density, the base layer can be adjusted higher appropriately.

### 3.2. Geometry optimization

After obtaining a large number of numerical simulation data as shown in Fig. 6, it is very interesting to use machine learning methods to accelerate the optimization of the combination of base layer and the degassing layer heights. The data-driven DNN model, which can be run within seconds, is far more computationally efficient than traditional physical models. Besides, owing to its powerful nonlinear fitting capability, the predictive accuracy can also be guaranteed. Therefore, if well trained, the DNN model can work as an accurate and efficient surrogate for physical model. To demonstrate the surrogate accuracy more directly, the squared correlation coefficient  $R^2$  is introduced to evaluate model performance and is defined by:

$$R^2 = 1 - \frac{\sum_{i=1}^n (t_i - \hat{t}_i)^2}{\sum_{i=1}^n (t_i - \bar{t}_i)^2} \quad (5)$$

where  $t_i$  and  $\hat{t}_i$  (s) are the detachment time of bubble obtained by the 3D physical model and the surrogate model, respectively. It can be seen that both values of  $R^2$  are over 0.98 for both training and testing datasets, as shown in Figs 7(a) and (b), which indicate that DNN can effectively learn disciplines from data generated by physical model, and replace it

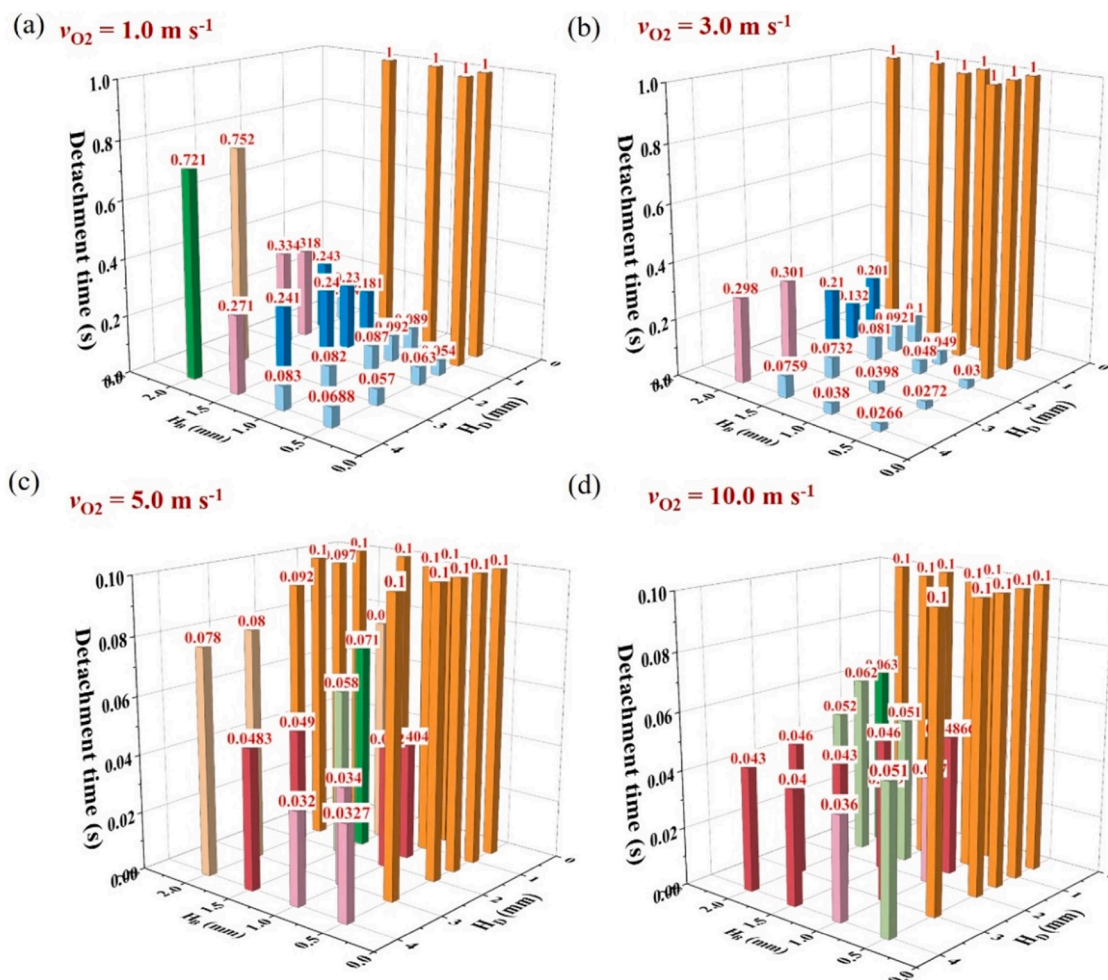


Fig. 6. Effect of degassing layer and base layer height on bubble detachment time under the different oxygen velocity.

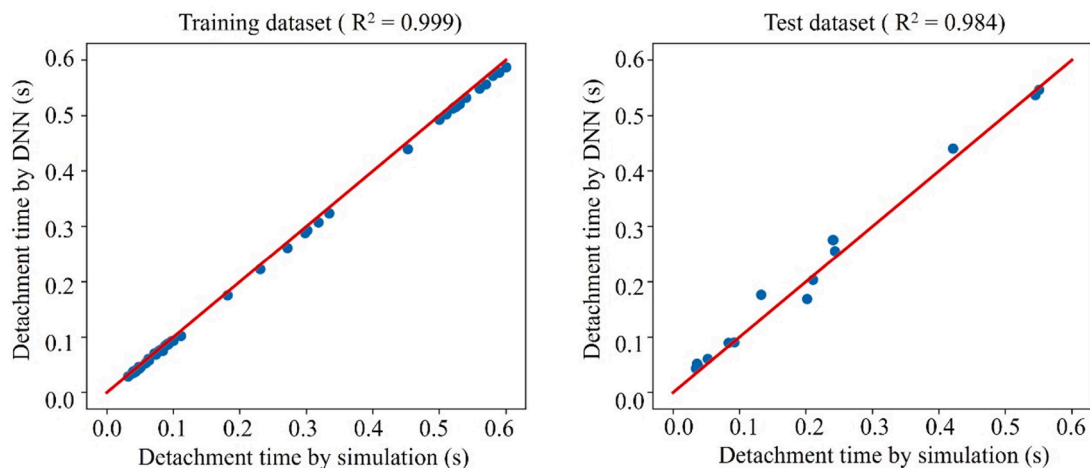


Fig. 7. Comparisons of the original data and predictions given by DNN.

in a highly efficient manner. Therefore, the trained DNN can be used to predict the bubble detachment time for different combinations of degassing layer and base layer heights. Finally, the optimal combinations of base layer and degassing layer predicted by GA are shown in Table 3. Although the actual optimal combination is almost impossible to determine due to the immeasurable number of simulation cases, the similarity of the GA optimization results to those of the 3D model can demonstrate that data-driven surrogate model for geometric optimization are feasible and reliable.

### 3.3. Experimental validation

The present optimal combination of degassing layer and base layer heights for the least bubble detachment time are predicted by the surrogate model. For verification, it would be better to conduct the further experiments to prove the feasibility of the optimization results and the proposed framework.

As shown in Fig. 8(a), iR-free cell voltage demonstrates that with a fixed 1 mm base layer height, the degassing layer of 3 mm shows better performance compared to that with 1 and 2 mm. Although the rib width of the base layer and the assembly torque of PEMWE are consistent in all cases, it is still difficult to guarantee the same ohmic losses, as depicted in Fig. 8 (b). Therefore, the effect of assembly needs to be excluded by means of iR-free cell voltage. The whole cell voltage and EIS under the different current densities are also provided in Fig. S2(Supporting Information). Through the two-phase flow visualization in Fig. 8(c), it can be observed that bubbles cannot detach from the electrode surface when the degassing layer is 1 mm, which shows the same conclusion with that in Fig. 4. As the degassing layer increases, two-phase flow regime in flow field has been changed significantly. Moreover, more outer surfaces of electrode in the base layer are exposed to water rather than covered by

bubbles due to the greatly reduced slug flow (also see Videos S1-S6 for visualization of two-phase flow regimes in flow field). Finally, both in terms of electrochemistry and two-phase flow visualization, the optimized combinations show obvious improvements in PEMWE.

## 4. Conclusion

In this study, we aim to conduct the further optimization for the proposed dual-layer flow field design in PEMWE through the combination of numerical simulation and machine learning methods. Firstly, the VOF (volume of fluid) method was utilized to investigate the effects of different degassing layer and base heights on the bubble behavior in channel and determine the time for the bubbles to detach from the electrode surface (bubble detachment time) in all cases. However, it is very time-consuming to get the optimal combination of base layer and degassing layer heights due to the large number of potential cases, which needs to be calculated through computation-intensive physical model. It was numerically found that when  $H_B$  is fixed, there is an optimal height for  $H_D$ . The reasoning also applies to  $H_B$ . In addition, the geometric parameters in the dual-layer design are easy to be characterized and bubble detachment is significantly affected by degassing layer height ( $H_D$ ), base layer height ( $H_B$ ) and oxygen velocity ( $v_{O_2}$ ), machine learning methods are very suitable to accelerate the optimization of this design. After that, a data-driven surrogate model, i.e., DNN, was developed and successfully trained using data obtained by the physical VOF method. Based on the highly efficient surrogate, GA was further utilized to determine the optimal heights of base layer and degassing layer. Finally, the reliability of the optimization was validated by bubble visualization in channel and electrochemical characterization in PEMWE through experiments. Therefore, this study successfully demonstrates the feasibility of the data-driven surrogate model in flow field design and optimization for PEMWE.

Table 3

Optimal combinations for the least bubble detachment time.

$v_{O_2}$ (m s <sup>-1</sup> )	Combination ( $H_B$ , $H_D$ )	Bubble detachment time (s)
1	(1, 2.5)	0.085
	(1, 3)	0.086
	(1, 3.5)	0.088
3	(1, 2.5)	0.046
	(1, 3)	0.043
	(1, 3.5)	0.042
5	(1, 2.5)	0.049
	(1, 3)	0.044
	(1, 3.5)	0.039
10	(1, 2.5)	0.039
	(1, 3)	0.042
	(1, 3.5)	0.045

### CRedit authorship contribution statement

**Lizhen Wu:** Writing – original draft, Investigation, Formal analysis, Data curation, Conceptualization. **Zhefei Pan:** Writing – original draft, Investigation. **Shu Yuan:** Writing – original draft, Investigation. **Xiaoyu Huo:** Writing – original draft. **Qiang Zheng:** Writing – original draft, Investigation, Formal analysis, Conceptualization. **Xiaohui Yan:** Writing – review & editing. **Liang An:** Writing – review & editing, Supervision, Funding acquisition.

### Declaration of competing interest

The authors declare that they have no known competing financial

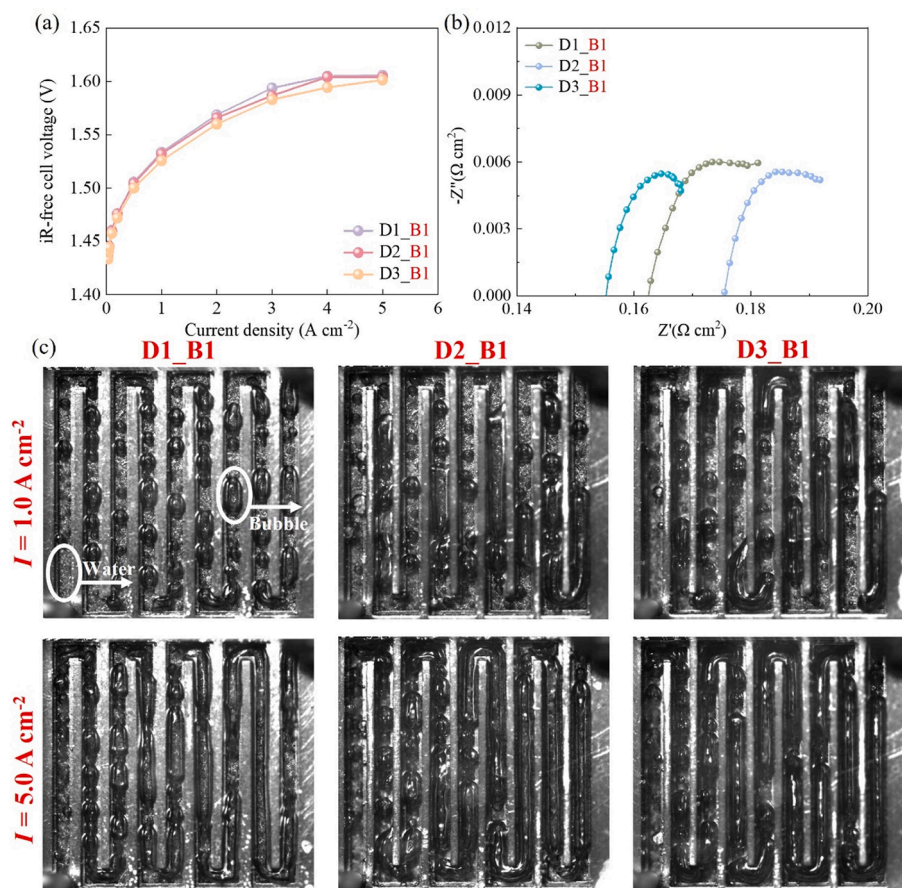


**Fig. 8.** Comparison of water electrolyzer with fixed base layer and different degassing layer on (a) iR-free cell voltage; (b) HFR measurement at  $3 \text{ A cm}^{-2}$ ; (c) two-phase flow regimes distribution in flow field.

interests or personal relationships that could have appeared to influence the work reported in this paper.

### Acknowledgements

The work described in this paper was supported by a grant from National Natural Science Foundation of China (No. 42302271), and a grant from the Research Grants Council of the Hong Kong Special Administrative Region, China (No. N\_PolyU559/21).

### Supplementary materials

Supplementary material associated with this article can be found, in the online version, at [doi:10.1016/j.egyai.2024.100411](https://doi.org/10.1016/j.egyai.2024.100411).

### References

- [1] Shiva Kumar S, Lim H. An overview of water electrolysis technologies for green hydrogen production. *Energy Reports* 2022;8:13793–813. <https://doi.org/10.1016/j.egyai.2022.10.127>.
- [2] Zainal BS, Ker PJ, Mohamed H, Ong HC, Fattah IMR, Rahman SMA, et al. Recent advancement and assessment of green hydrogen production technologies. *Renewable and Sustainable Energy Reviews* 2024;189:113941. <https://doi.org/10.1016/j.rser.2023.113941>.
- [3] Wang B, Ni M, Zhang S, Liu Z, Jiang S, Zhang L, et al. Two-phase analytical modeling and intelligence parameter estimation of proton exchange membrane electrolyzer for hydrogen production. *Renewable Energy* 2023;211:202–13. <https://doi.org/10.1016/j.renene.2023.04.090>.
- [4] Günay ME, Tapan NA. Analysis of PEM and AEM electrolysis by neural network pattern recognition, association rule mining and LIME. *Energy and AI* 2023;13:100254. <https://doi.org/10.1016/j.egyai.2023.100254>.
- [5] Tang J, Su C, Shao Z. Advanced membrane-based electrode engineering toward efficient and durable water electrolysis and cost-effective seawater electrolysis in membrane electrolyzers. *Exploration* 2024;4:20220112. <https://doi.org/10.1002/EXP.20220112>.
- [6] Maier M, Smith K, Dodwell J, Hinds G, Shearing PR, Brett DJL. Mass transport in PEM water electrolyzers: A review. *International Journal of Hydrogen Energy* 2022;47:30–56. <https://doi.org/10.1016/j.ijhydene.2021.10.013>.
- [7] Hu K, Zhong Z, Huang D, Wang C, Ying Y, Ai X, et al. Optimal design of the diphasic flow pattern in water electrolyzers with CFD-independent multiphysics model. *Energy Conversion and Management* 2023;296:117674. <https://doi.org/10.1016/j.enconman.2023.117674>.
- [8] Yuan S, Zhao C, Mei X, Shen S, Wang Q, Yan X, et al. Bubble management in PEM water electrolysis via imprinting patterned grooves on catalyst layer. *International Journal of Heat and Mass Transfer* 2023;212:124249. <https://doi.org/10.1016/j.ijheatmasstransfer.2023.124249>.
- [9] Yuan S, Zhao C, Cai X, An L, Shen S, Yan X, et al. Bubble evolution and transport in PEM water electrolysis: Mechanism, impact, and management. *Progress in Energy and Combustion Science* 2023;96:101075. <https://doi.org/10.1016/j.pecs.2023.101075>.
- [10] Zhang T. Relationship of local current and two-phase flow in proton exchange membrane electrolyzer cells. *Journal of Power Sources* 2022;542:231742. <https://doi.org/10.1016/j.jpowsour.2022.231742>.
- [11] Majasan JO. Two-phase flow behaviour and performance of polymer electrolyte membrane electrolyzers: Electrochemical and optical characterisation. *International Journal of Hydrogen Energy* 2018;15659–72. <https://doi.org/10.1016/j.ijhydene.2018.07.003>.
- [12] Yuan S, Zhao C, Fu C, Li J, Su Y, Xue R, et al. Discovery of bubble accumulation behavior in catalyst layer of proton exchange membrane water electrolyzer. *International Journal of Heat and Mass Transfer* 2024;227:125552. <https://doi.org/10.1016/j.ijheatmasstransfer.2024.125552>.
- [13] Lin R, Lu Y, Xu J, Huo J, Cai X. Investigation on performance of proton exchange membrane electrolyzer with different flow field structures. *Applied Energy* 2022;326:120011. <https://doi.org/10.1016/j.apenergy.2022.120011>.
- [14] Pan Z, Xie F, Zhang Z, Zhao Z, Wu L, Li W, et al. Overall Design of a Gradient-Ordered Membrane Electrode Assembly for Direct Liquid Fuel Cells. *Adv Funct Materials* 2024;2404710. <https://doi.org/10.1002/adfm.202404710>.
- [15] Wu L, Pan Z, Yuan S, Shi X, Liu Y, Liu F, et al. A dual-layer flow field design capable of enhancing bubble self-pumping and its application in water electrolyzer. *Chemical Engineering Journal* 2024;488:151000. <https://doi.org/10.1016/j.cej.2024.151000>.

- [16] Wang K, Wang Y, Yu Z, Xiao F, Ta L, Ye F, et al. Multi-technique experimental characterization of a PEM electrolyzer cell with interdigitated-jet hole flow field. *Energy Conversion and Management* 2024;306:118276. <https://doi.org/10.1016/j.enconman.2024.118276>.
- [17] Mohamed A, Ibrahim H, Kim K. Machine learning-based simulation for proton exchange membrane electrolyzer cell. *Energy Reports* 2022;8:13425–37. <https://doi.org/10.1016/j.egy.2022.09.135>.
- [18] Günay ME. Analysis and modeling of high-performance polymer electrolyte membrane electrolyzers by machine learning. *International Journal of Hydrogen Energy* 2022;2134–51. <https://doi.org/10.1016/j.ijhydene.2021.10.191>.
- [19] Khatib FN, Wilberforce T, Thompson J, Olabi AG. Experimental and analytical study of open pore cellular foam material on the performance of proton exchange membrane electrolyzers. *International Journal of Thermofluids* 2021;9:100068. <https://doi.org/10.1016/j.ijft.2021.100068>.
- [20] Ding R, Chen Y, Rui Z, Hua K, Wu Y, Li X, et al. Machine learning utilized for the development of proton exchange membrane electrolyzers. *Journal of Power Sources* 2023;556:232389. <https://doi.org/10.1016/j.jpowsour.2022.232389>.
- [21] André C-G. Deep learning-enhanced characterization of bubble dynamics in proton exchange membrane water electrolyzers. *Physical Chemistry Chemical Physics* 2024;26:14529–37. <https://doi.org/10.1039/D3CP05869G>.
- [22] Salari A. Optimization of a solar-based PEM methanol/water electrolyzer using machine learning and animal-inspired algorithms. *Energy Conversion and Management* 2023;283:116876. <https://doi.org/10.1016/j.enconman.2023.116876>.
- [23] Sawada S. Toward the design of graft-type proton exchange membranes with high proton conductivity and low water uptake: A machine learning study. *Journal of Membrane Science* 2024;692:122169. <https://doi.org/10.1016/j.memsci.2023.122169>.
- [24] Zhang G, Wu L, Jiao K, Tian P, Wang B, Wang Y, et al. Optimization of porous media flow field for proton exchange membrane fuel cell using a data-driven surrogate model. *Energy Conversion and Management* 2020;226:113513. <https://doi.org/10.1016/j.enconman.2020.113513>.
- [25] Wang B, Zhang G, Wang H, Xuan J, Jiao K. Multi-physics-resolved digital twin of proton exchange membrane fuel cells with a data-driven surrogate model. *Energy and AI* 2020;1:100004. <https://doi.org/10.1016/j.egyai.2020.100004>.
- [26] Hayatzadeh A, Fattahi M, Rezaveisi A. Machine learning algorithms for operating parameters predictions in proton exchange membrane water electrolyzers: Anode side catalyst. *International Journal of Hydrogen Energy* 2024;56:302–14. <https://doi.org/10.1016/j.ijhydene.2023.12.149>.
- [27] Yang R, Mohamed A, Kim K. Optimal design and flow-field pattern selection of proton exchange membrane electrolyzers using artificial intelligence. *Energy* 2022; 264:126135. <https://doi.org/10.1016/j.energy.2022.126135>.
- [28] Chen J, Lv H, Shen X, Zhang C. Multi-objective optimization design and sensitivity analysis of proton exchange membrane electrolytic cell. *Journal of Cleaner Production* 2024;434:140045. <https://doi.org/10.1016/j.jclepro.2023.140045>.
- [29] Wu L, An L, Jiao D, Xu Y, Zhang G, Jiao K. Enhanced oxygen discharge with structured mesh channel in proton exchange membrane electrolysis cell. *Applied Energy* 2022;323:119651. <https://doi.org/10.1016/j.apenergy.2022.119651>.
- [30] Wu L, Zhang G, Xie B, Tongsh C, Jiao K. Integration of the detailed channel two-phase flow into three-dimensional multi-phase simulation of proton exchange membrane electrolyzer cell. *International Journal of Green Energy* 2021;18: 541–55. <https://doi.org/10.1080/15435075.2020.1854270>.
- [31] Kingma DP, Ba J. Adam: A Method for Stochastic Optimization 2017.
- [32] Zou X, Lu Q, Wu J, Zhang K, Tang M, Wu B, et al. Screening Spinel Oxide Supports for RuO<sub>2</sub> to Boost Bifunctional Electrocatalysts for Advanced Zn–Air Batteries. *Adv Funct Materials* 2024;2401134. <https://doi.org/10.1002/adfm.202401134>.
- [33] Pan Z, Zhang Z, Li W, Huo X, Liu Y, Esan OC, et al. Development of a High-Performance Ammonium Formate Fuel Cell. *ACS Energy Lett* 2023;8:3742–9. <https://doi.org/10.1021/acscenergylett.3c01165>.
- [34] Wang Y, Seo B, Wang B, Zamel N, Jiao K, Adroher XC. Fundamentals, materials, and machine learning of polymer electrolyte membrane fuel cell technology. *Energy and AI* 2020;1:100014. <https://doi.org/10.1016/j.egyai.2020.100014>.